Wear-out Failure Analysis of an Impedance-Source PV Microinverter Based on System-Level Electrothermal Modeling

Shen, Yanfeng; Chub, Andrii; Wang, Huai; Vinnikov, Dmitri; Liivik, Elizaveta; Blaabjerg, Frede

Published in:
I E E E Transactions on Industrial Electronics

DOI (link to publication from Publisher):
10.1109/TIE.2018.2831643

Publication date:
2019

Document Version
Accepted author manuscript, peer reviewed version

Wear-out Failure Analysis of an Impedance-Source PV Microinverter Based on System-Level Electro-Thermal Modeling

Yanfeng Shen, *Student Member, IEEE,* Andrii Chub*, Member, IEEE,*
Huai Wang, *Senior Member*, *IEEE*, Dmitri Vinnikov*, Senior Member, IEEE,*
Elizaveta Liivik*, Member, IEEE*, and Frede Blaabjerg, *Fellow*, *IEEE*.

***Abstract*—The wear-out performance of an impedance-source photovoltaic (PV) microinverter (MI) is evaluated and improved based on two different mission profiles. The operating principle and hardware implementation of the MI are firstly described. With the experimental measurements on a 300-W MI prototype and system-level finite element method (FEM) simulations, the electro-thermal models are built for the most reliability-critical components, i.e., power semi-conductor devices and capacitors. The dependence of the power loss on the junction/hotspot temperature is considered, the enclosure temperature is taken into account, and the thermal cross-coupling effect between components is modeled. Then the long-term junction/ hotspot temperature profiles are derived and further translated into components' annual damages with the lifetime and damage accumulation models. After that, the Monte Carlo simulation and Weibull analysis are conducted to obtain the system wear-out failure probability over time. It reveals that both the mission profile and the thermal cross-coupling effect have a significant impact on the prediction of system wear-out failure, and the dc-link electrolytic capacitor is the bottleneck of long-term reliability. Finally, the multi-mode control with a variable dc-link voltage is proposed, and a more reliable dc-link electrolytic capacitor is employed, which results in a remarkable reliability improvement for the studied PV MI.**

***Index Terms*—PV microinverter, reliability, wear out, electro-thermal modeling**

Manuscript received Dec. 10, 2017; revised Mar. 22, 2018; accepted Apr. 17, 2018. This work was supported in part by the Innovation Fund Denmark through the Advanced Power Electronic Technology and Tools (APETT) project, in part by the Estonian Centre of Excellence in Zero Energy and Resource Efficient Smart Buildings and Districts under Grant 2014-2020.4.01.15-0016, in part by the European Regional Development Fund, and in part by the Estonian Research Council under project PUT1443. *(Corresponding author: Yanfeng Shen)*

Yanfeng Shen, Huai Wang, Elizaveta Liivik, and Frede Blaabjerg are with the Department of Energy Technology, Aalborg University, 9220 Aalborg, Denmark (e-mail: yaf@et.aau.dk, hwa@et.aau.dk, liisa.liivik@ttu.ee, fbl@et.aau.dk).

Andrii Chub is with the Department of Electrical Power Engineering and Mechatronics, Tallinn University of Technology, 19086 Tallinn, Estonia (e-mail: andrii.chub@ttu.ee).

Dmitri Vinnikov is with the Department of Electrical Power Engineering and Mechatronics, Tallinn University of Technology, 19086 Tallinn, Estonia, and is also with Ubik Solutions LLC, 11911 Tallinn, Estonia (e-mail: dmitri.vinnikov@ttu.ee).

Color versions of one or more of the figures in this paper are available online at http://ieeexplore.ieee.org.

I. Introduction

Over the last decade, the solar photovoltaic (PV) energy continues to experience a significant growth tendency due to the dramatic price reduction of PV modules in the world market [1], and the progressive evolution of PV converters whose efficiency has been reported as high as 99% [2].

Compared to the central and string PV inverters, the microinverters (MIs) feature more advantages in low power applications such as module-level maximum power point tracking (MPPT), low PV-system installation effort, and easy condition monitoring and failure detection [3]-[5]. However, there are also some challenges for PV MIs. First, the MIs are normally cooled by natural convection and they are installed close to the PV module, which means that they can be subjected to a more extreme environment than central inverters typically located in climate controlled environment [6]-[7]. In addition, there is a trend that the MI will be incorporated into the module frame in the future [6]. The lifetime/warranty of PV modules is about 25 years, but the inverters have to be replaced every 5 to 10 years [8]; this implies that the lifetime of the MIs needs to be extended to match that of the PV modules. Therefore, reliability evaluation and reliability-oriented design of PV MIs under a harsh environment is paramount [9]-[10].

Recently, increasing efforts have been made to the power electronics reliability, especially to discrete components or modules (e.g., IGBT, MOSFET, and capacitor) [10]-[20]. Only a few works [10], [13], [19] focus on the system-level reliability but not for PV module-level power electronics (MLPE). In addition, one significant drawback of previous general reliability assessments is that the local ambient temperature and the thermal cross-coupling effect between components are not considered; thus, the reliability performance might be overestimated. Based on a failure mode and effects analysis (FMEA) survey for MLPE products [21], the loose connection of dc input and ac output connectors, wear-out of dc-link electrolytic capacitors, varistor failure-short from the surge, and degradation of MOSFETs and diodes are identified as the top four failure modes; meanwhile, temperature cycling is reported as the most important stressor that affects the reliability of MLPE products. Only a few studies focused on the MI reliability can be found in literature, and most of them use the MIL-HDBK-217 handbook [22] to determine the failure rates of MIs [20]. Unfortunately, the constant failure rates only describe the large-population statistics of random failures, and the wear-out failure is not considered. Meanwhile, the MLPE

This article has been accepted for publication in a future issue of this journal, but has not been fully edited. Content may change prior to final publication. Citation information: DOI 10.1109/TIE.2018.2831643, IEEE Transactions on Industrial Electronics

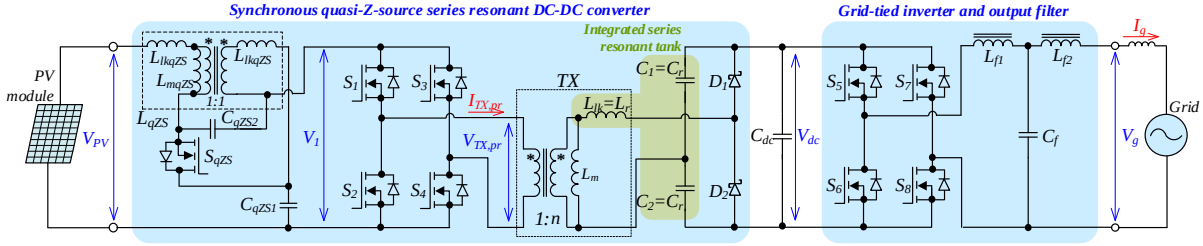

Fig. 1. Schematic of the impedance-source PV microinverter.

Fig. 2. Photo of the built PV microinverter prototype.

market is relatively nascent and there is not enough long-term usage data or independent reliability testing; therefore, accelerated testing of PV MI products is conducted in [6] for a long-term reliability prediction. It turns out that the time-to-failure of MIs from different manufacturers deviates significantly due to the design.

The PV MI system demands a wide input voltage and load regulation range at high DC voltage gains [23]. The impedance-source converters featuring the immunity to shoot-through and open states, continuous input current, low inrush current, buck-boost functionality as well as high control flexibility, and thus have recently gained much attention [24]-[25]. In [26], a quasi-Z-source series resonant dc-dc converter (qZSSRC) is proposed for MLPE applications; with a multimode control, the qZSSRC is capable of maintaining high efficiency within the six-fold variation of the input voltage (10~60 V). This feature enables the implementation of the shade-tolerant (global) MPPT, thus ensuring the maximum possible energy yield from the PV module even when two out of three substrings are shaded or in the conditions of opaque shading which could be caused by the fallen leaves or bird droppings [27]. Alternatively to the shoot-through pulse width modulation (PWM) and phase-shift modulation (PSM) in [26], the qZSSRC could also be controlled by the asymmetrical PWM [28], variable frequency [29] or the topology morphing [30], which significantly widens gain range and increases application flexibility.

Although the impedance-source converters properly match the demanding requirements of the PV MLPE application, their reliability performance is an open question. This paper aims to investigate the wear-out failure of an impedance-source PV MI. A mission profile based system-level wear-out assessment method is proposed and applied. A detailed electro-thermal model is built with the aid of system-level finite element method (FEM) simulations and experimental measurements on a 300-W MI prototype. Then, the mission profiles are translated into long-term junction/hotspot temperature profiles and annual damages for components. The Monte Carlo simulation and Weibull analysis are conducted to obtain the system wear-out failure over time. Finally, the variable dc-link voltage control is applied and the electrolytic capacitor is replaced with a more reliable one to improve system reliability. Compared with conventional reliability assessments, several improvements are made: 1) the dependence of component power loss on the junction/hotspot temperature is experimentally characterized and applied; 2) system-level FEM simulations are performed and the enclosure temperature is incorporated into the electro-thermal model; 3) the thermal cross-coupling effect between components is considered and modeled.

II. System Description and Reliability Evaluation

A. System Description

The schematic of the impedance-source PV MI is shown in Fig. 1. The two-stage MI consists of the quasi-Z-source series resonant dc-dc converter (qZSSRC) and the full-bridge inverter. The detailed operation principle and parameter design guidelines have been presented in [26]. There are three operation modes for the front-end qZSSRC:

1) Pass-Through Mode (PTM): The qZSSRC operates as the series-resonant converter (SRC) in the DC transformer mode. The normalized DC voltage gain is unity [26]:

$$G_{PTM} = \frac{V_{dc}}{2nV_{PV}} = 1 \tag{1}$$

2) Buck Mode: The operation of the qZSSRC is similar to that of the SRC with phase-shift modulation (PSM) control at the resonant frequency and discontinuous resonant current. The latter is due to small leakage inductance values of conventional transformers ($Q \ll 1$). The normalized DC voltage gain depends on the phase shift angle φ and the quality factor Q as in [26]:

$$G_{buck(DCM)} = \frac{V_{dc}}{2nV_{PV}} = 0.5\left(AB + \sqrt{A^2B^2 + A\frac{8}{\pi Q}}\right) \tag{2}$$

where $A = (1-\cos[\pi(1-\varphi/180)])/2$, $B = 2/(\pi Q) - 1$, and $Q = (8\pi f_{sw} L_{lk} P_{dc})/V_{dc}^2$.

3) Boost Mode: the voltage is controlled by shoot-through pulse width modulation (ST-PWM) implemented as a symmetrical overlap of active states. The normalized DC voltage gain in this mode depends on the shoot-through duty cycle D_{ST} [26]:

$$G_{boost} = \frac{V_{DC}}{2nV_{PV}} = \frac{1}{1-2D_{ST}}. \tag{3}$$

A 300-W PV MI prototype, consisting of the main circuit, auxiliary power supply circuit and microcontroller unit (MCU), has been built, as shown in Fig. 2. The detailed specifications and parameters are given in Table I. The measured full-load waveforms and efficiency curves at different input voltages and power levels are shown in Fig. 3.

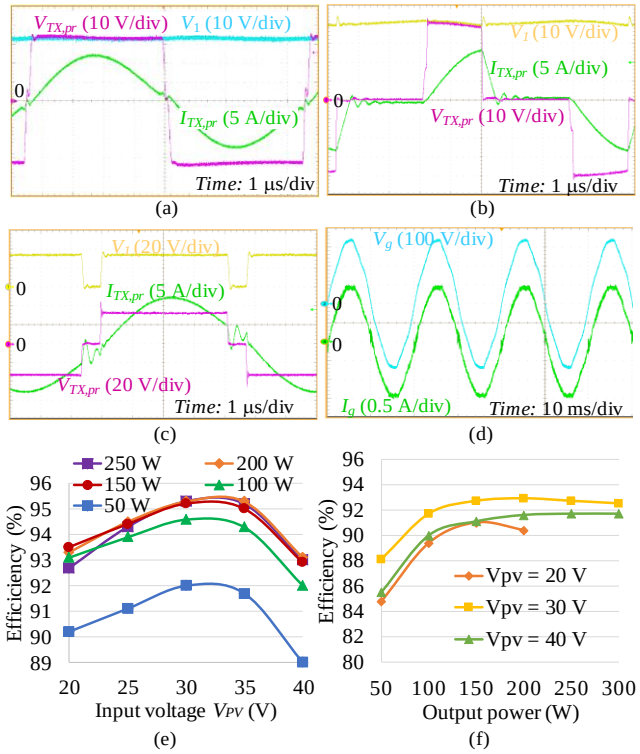

Fig. 3. Experimental waveforms in the (a) pass-through mode, (b) buck mode, and (c) boost mode. (d) Measured grid voltage and current waveforms. Measured efficiency curves of (e) the dc-dc stage and (f) the whole microconverter including the auxiliary power supply.

TABLE I
SPECIFICATIONS AND PARAMETERS OF THE MICROINVERTER PROTOTYPE

Descriptions	Parameters
Input voltage range	10–60 V
Nominal voltage	33 V
Most probable operating voltage range	20–40 V
Rated power	300 W
Switch. frequency of dc-dc stage	110 kHz
Switch. frequency of inverter stage	20 kHz
Switches S_{qZS}, S_1…S_4	BSC035N10NS5
Switches S_5…S_8	SCT2120AFC
Diodes D_1…D_2	C3D02060E
Capacitors C_{qZS1} and C_{qZS2}	2.2 μF × 12, C1210C225K1R
Coupled inductor L_{qZS}	L_{mqZS}=12 μH, L_{lkqZS}=0.6 μH, custom
Resonant capacitors C_1 and C_2	10 nF // 33 nF, MKP1840310104M and B32672Z6333K
DC-link capacitor C_{dc}	150 μF, 500-V electrolytic capacitor
Grid-side LCL filter: capacitor C_f	470 nF, B32653A6474K
Inductors L_{f1}	2.6 mH, custom
Inductors L_{f2}	1.8 mH, custom
Transformer TX	L_m=1 mH, L_{lk}=24 μH, n=6, custom

B. Reliability Evaluation Process

The failure modes of a power electronics system include the hardware failure, software failure and human error [10], as shown in Fig. 4. The hardware failure consists of the catastrophic, random, burn-in and wear-out failures. According to the FMEA survey for MLPE products in [21], connector contact failure, wear-out of electrolytic capacitor, short-circuit of varistor, and degradation of MOSFET/diode are reported as the top-four frequently happened failure modes, and the temperature cycling is identified as the most critical stressor affecting reliability. Therefore, this paper evaluates the wear-out failure of critical components, i.e., power semiconductors and capacitors, based on the flowchart illustrated in Fig. 4.

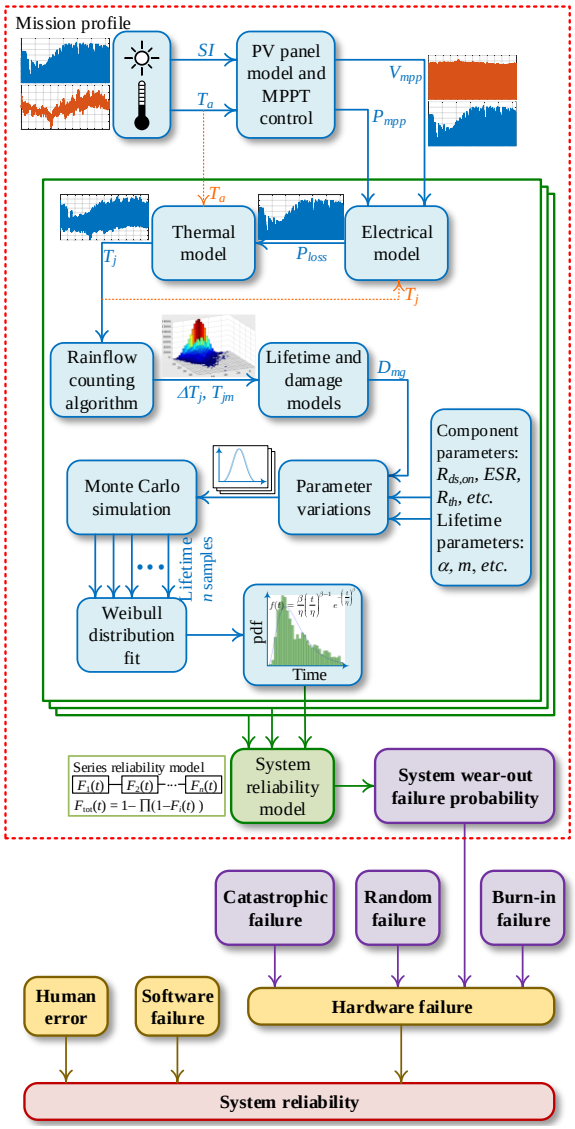

Fig. 4. Failure modes of power electronics systems and evaluation flowchart of the hardware wear-out failure probability.

The real-field mission profile, i.e., the solar irradiance (SI) and ambient temperature T_a for the PV MI system, directly determines the electrical and thermal loadings, and thus affects the degradation process of the components. With a PV panel model and an MPPT control, the long-term mission profile can be translated into the real-time voltage and power at the maximum power point, $V_{PV(mpp)}$ and $P_{PV(mpp)}$, which are the input of the MI. The power loss and junction/hotspot temperature of a component can be subsequently calculated based on the electrical and thermal models. The rainflow counting algorithm [31] is employed to extract the number of temperature cycles with different characteristics (e.g., the mean junction temperature T_{jm}, and the temperature swing ΔT_j). After that, the lifetime and damage accumulation models can be used to estimate the accumulated damage over a year. The junction/hotspot temperature T_j also affects the power loss, which is taken into account. When the damage is accumulated to 1, it is assumed that the component fails. Then the static wear-out lifetime of a component can be derived. In the real world, however, the parameters of the component and lifetime models have variations, which would affect the distribution of wear-out

This article has been accepted for publication in a future issue of this journal, but has not been fully edited. Content may change prior to final publication. Citation information: DOI 10.1109/TIE.2018.2831643, IEEE Transactions on Industrial Electronics

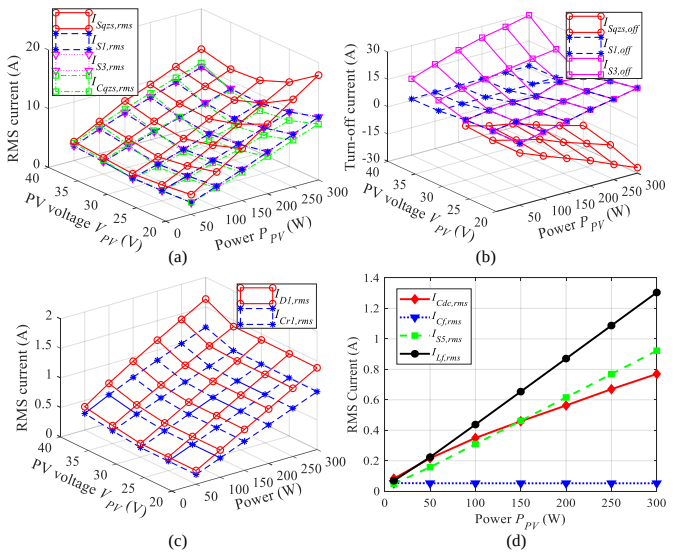

Fig. 5. Measured current characteristics of critical components. (a) RMS and (b) off-switching currents of primary-side components in the dc-dc stage; (c) RMS currents of secondary-side devices in the dc-dc stage; (d) RMS currents of inverter-stage devices.

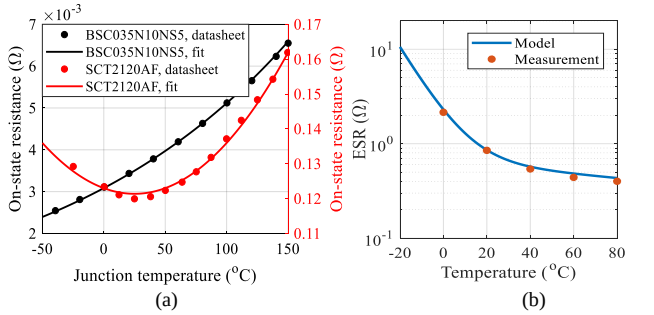

Fig. 6. Temperature characteristics of MOSFETs and an electrolytic capacitor. (a) Dependence of the on-state resistance $R_{ds,on}$ on the junction temperature for MOSFETs. (b) Dependence of ESR (at 100 Hz) on the hotspot temperature for the aluminum electrolytic capacitor used in the prototype.

failure probability. Therefore, a sensitivity analysis—Monte Carlo simulation is conducted based on a large population of samples. With the Weibull distribution fitting, the probability density function (pdf) for each component can be derived; and the system wear-out failure probability finally can be obtained with the reliability model for a series connected system.

III. Electro-Thermal and Lifetime Modeling of Critical Components

A. Power Loss Modeling

1) Power Semiconductor Devices

The current stress characteristics are measured for critical components, as shown in Fig. 5. The power loss of MOSFETs consists of the conduction loss $P_{T,con}$, turn-on loss $P_{T,on}$, and turn-off loss $P_{T,off}$. The conduction loss calculation is straight-forward, i.e., $P_{T,con} = I_{T,rms}^2 R_{ds,on}$, where $I_{T,rms}$ is the root-mean-square (RMS) current flowing through the MOSFET and $R_{ds,on}$ represents its on-state resistance which is a function of the junction temperature (cf. Fig. 6(a)). For the MOSFETs (S_{qZS}, S_1-S_4) in the dc-dc converter stage, their soft-switching conditions depend on the operation modes, as illustrated in [26]. For the inverter stage, the unipolar modulation is applied and the MOSFETs are hard-switched. The switching losses of MOSFETs are calculated with the model given in [32]. Two SiC Schottky diodes C3D02060E are employed for D_1-D_2, and the conduction loss is derived by $P_{D,con} = I_{D,avg} V_{D0} + I_{D,rms}^2 R_{D,on}$, where $V_{D0} = 0.98 - 0.0011 \times T_{jD}$, $R_{D,on} = 0.18 + 0.0018 \times T_{jD}$ [33], and T_{jD} is the junction temperature of the diode.

2) Capacitors

For the MI, the instantaneous power $p(t)$ contains a fluctuating power at twice the line frequency, which is decoupled by the dc-link capacitor C_{dc}. The electrical stresses over C_{dc} can be calculated by [34]

$$\Delta V_{dc} \approx P / (\omega_0 C_{dc} V_{dc}),\ I_{Cdc,rms} = P / (\sqrt{2} V_{dc}) \quad (4)$$

where P is the average power injected to the grid, ΔV_{dc} is the peak-to-peak ripple of the capacitor voltage V_{dc}, and $I_{Cdc,rms}$ is the RMS current flowing through C_{dc}. The aluminum electrolytic dc-link capacitor C_{dc} can be modeled as an ideal capacitor in series with an equivalent series resistor (ESR) [34]-[35]. There are two degradation mechanisms for the electrolytic capacitors [9]: chemical reactions due to electrolyte evaporation and contaminants, leading to deterioration of the dielectric material; localized heating, ion transport, and chemical processes caused by the leakage current [36]. The main stressor is the internal hotspot temperature T_h that is determined by the power loss $P_{Cdc,loss} = I_{Cdc,rms}^2 \cdot ESR(T_h)$. The ESR of an electrolytic capacitor is temperature dependent [37]-[38]; the temperature characteristic of the used electrolytic capacitor is measured and modeled as shown in Fig. 6(b).

For the ceramic and film capacitors (C_{qzs}, C_{r1}-C_{r2} and C_f), their power losses can be calculated in a similar way. However, their temperature characteristics are different from electrolytic capacitors. For the polypropylene film capacitors, the dependency of their capacitance on the temperature is very weak (0.023%/°C); in the meanwhile, the dissipation factor (DF) is largely unaffected by temperature [39]-[40]. Similarly, when the hotspot temperature is increased from 0 °C to 100 °C, the capacitance and DF of X7R ceramic capacitors decrease by only 5% and 1.5%, respectively [41]. Therefore, the impact of hotspot temperature on the power losses of polypropylene film and X7R ceramic capacitors are neglected in this paper.

3) Magnetic Components

The power losses of magnetic components consist of the core loss and the winding loss. The improved generalized Steinmetz equation (iGSE) [42] describes core loss, and the winding loss can be obtained with the Dowell model [43]-[44]. All the magnetic components were implemented with the Ferrite core 3C95 whose power loss density curve is flat with respect to temperature; this holds for various conditions of frequency and flux density [45]. Hence, the temperature dependence of the power losses in magnetic components is neglected.

B. Thermal Modeling

The PV MI is built with a four-layer PCB and is enclosed in an aluminum case (200 mm×150mm×45mm) by natural cooling. The case is filled up with elastic 2-component polyurethane casting compound [46] whose thermal conductivity (0.7 W/(K·m)) is almost 30 times higher than that of still air. Thus, the thermal cross-coupling effect between components (heat sources) cannot be neglected. However, most manufacturers provide the junction/core-ambient or case-ambient thermal resistance of a single component in a specific cooling condition.

This article has been accepted for publication in a future issue of this journal, but has not been fully edited. Content may change prior to final publication. Citation information: DOI 10.1109/TIE.2018.2831643, IEEE Transactions on Industrial Electronics

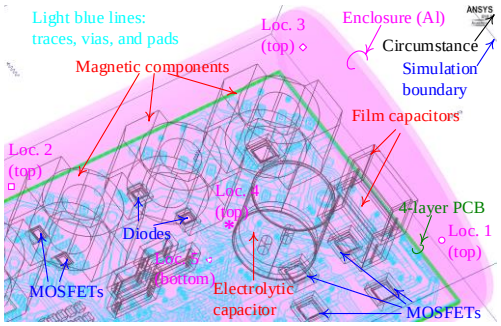

Fig. 7. Structure models of the main components, enclosure and PCB (including traces and vias) built in ANSYS/Icepak for FEM simulations. The PCB and the enclosure are placed horizontally. The enclosure is naturally cooled, i.e., all faces are exposed to the open air.

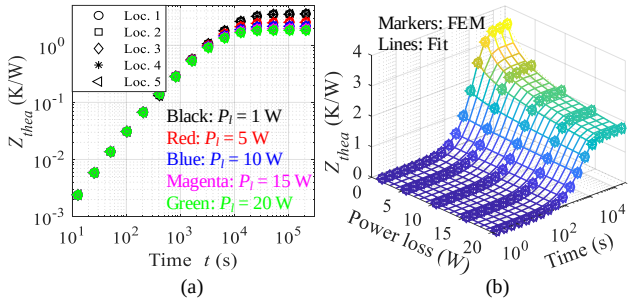

Fig. 8. (a) FEM simulated and (b) fitted enclosure-to-ambient thermal impedance at different power loss levels and enclosure locations.

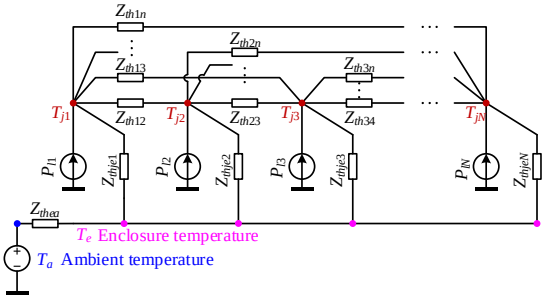

Fig. 9. Thermal impedance network of an enclosed converter system, including the self and mutual junction-enclosure thermal impedances.

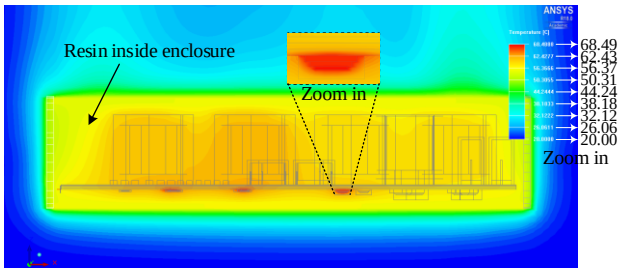

Fig. 10. FEM thermal simulation results in the case of total power loss $P_{l,tot}$ = 17.5 W. Temperature contour plane cut in the front view.

Apparently, these values cannot be used in the thermal analysis. Also, the mutual thermal resistance (thermal cross-coupling) depends on the heat transfer medium and the geometry/layout of components. Therefore, system-level FEM simulations are conducted to extract the self and mutual thermal resistances.

1) Enclosure-to-Ambient Thermal Impedance

The heat conduction, convection and radiation all exist in the thermal transfer from the enclosure to the circumstance. The heat transfer rate of convection is related to the temperature gap between the surface and the circumstance, whereas radiation intensity depends on the absolute temperature [47]-[48].

The enclosure of the studied MI is a custom hollow elliptical cylinder (cf. Fig. 7), which makes it difficult to analytically obtain the enclosure-to-ambient thermal impedance Z_{thea}. Therefore, multiple FEM simulations with ANSYS/Icepak are conducted at different power loss values and enclosure points, as shown in Fig. 8(a). It can be seen that the enclosure location has a negligible impact on Z_{thea}, i.e., it is almost isothermal, as the Aluminum and the filled compound have a high thermal conductivities. The enclosure-to-ambient thermal impedance Z_{thea} is a function of the total power loss of the MI, P_l, as well as time, and can be fitted as a first-order Foster model (cf. Fig.8(b))

$$Z_{thea} = R_{thea}(1 - \mathrm{e}^{-t/(R_{thea}C_{thea})}) \quad (5)$$

where C_{thea} is found to be constant as 2673 J/ºC but R_{thea} is a function of the total power loss, $R_{thea} = 3.5P_l^{-0.216}$. It should be noted that the enclosure is placed horizontally in all the FEM simulations above. If the microinverter is installed vertically in practice, then the FEM-simulated thermal resistance is found as $R_{thea} = 3.45P_l^{-0.213}$ which is very close to that in the horizontal orientation. Hence, for this custom aluminum enclosure, it can be assumed that the enclosure-to-ambient thermal impedance Z_{thea} is independent of its orientation.

2) Junction-to-Enclosure Thermal Impedance Network

Thermal resistance network of a converter with N main components (heat sources) is shown in Fig. 9. The mutual thermal impedance is present between the components. It is difficult to perform the analytical calculation because of the irregular geometry of heat transfer medium. Conduction is the main heat transfer way inside the compound-filled converter, i.e., the components and compound inside the enclosure form a linear and time-invariant (LTI) system [49]. Therefore, the superposition principle can be applied [50]-[51] and the junction temperature for each component can be obtained by

$$\begin{bmatrix} T_{j1}(t) \\ T_{j2}(t) \\ \vdots \\ T_{jN}(t) \end{bmatrix} = \frac{\mathrm{d}}{\mathrm{d}t} \begin{bmatrix} Z_{je11}(t) & Z_{je12}(t) & \cdots & Z_{je1N}(t) \\ Z_{je21}(t) & Z_{je22}(t) & \cdots & Z_{je2N}(t) \\ \vdots & \vdots & \ddots & \vdots \\ Z_{jeN1}(t) & Z_{jeN2}(t) & \cdots & Z_{jeNN}(t) \end{bmatrix} * \begin{bmatrix} P_{l1}(t) \\ P_{l2}(t) \\ \vdots \\ P_{lN}(t) \end{bmatrix} + T_e \quad (6)$$

where T_{ji} is the junction/hotspot temperature of component i, Z_{jenn} represents the self junction/hotspot-to-enclosure thermal impedance, Z_{jemn} denotes the mutual junction/hotspot-to-enclosure thermal impedance between components m and n, T_e is the enclosure temperature, P_{ln} is the power loss of the nth component, and "*" denotes convolution.

Detailed structure models for all main components, enclosure, and PCB (including traces and vias) are built in ANSYS/Icepak based on real dimensions and material properties, as shown in Fig.7. To extract the thermal impedances in (6), multiple system-level FEM simulations are conducted, as shown in Fig. 10. It can be seen that the local ambient temperature of each component has no significant difference due to the filled compound. The self thermal impedance of S_1 and mutual thermal impedances between S_1 and other components are depicted in Fig. 11(a). The

This article has been accepted for publication in a future issue of this journal, but has not been fully edited. Content may change prior to final publication. Citation information: DOI 10.1109/TIE.2018.2831643, IEEE Transactions on Industrial Electronics

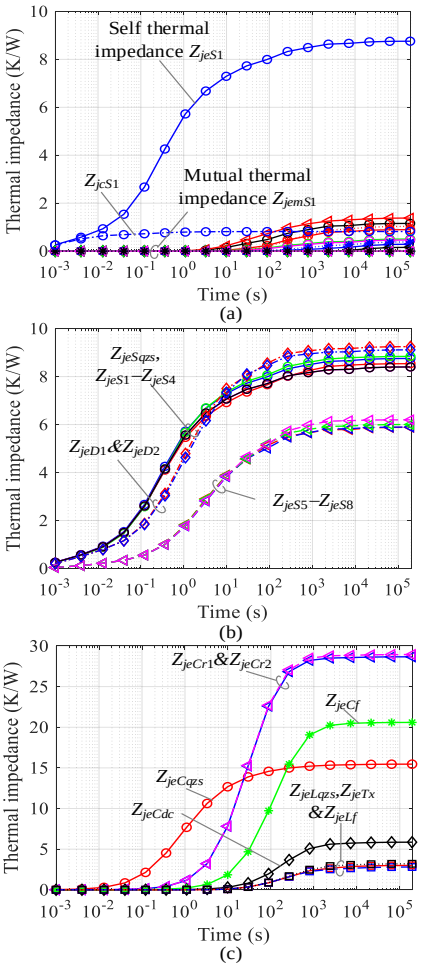

Fig. 11. FEM simulation results for thermal impedances. (a) Junction-case and junction-enclosure thermal impedances of *S*1; mutual junction-enclosure thermal impedances between *S*1 and other components. Self junction-enclosure thermal impedances of (b) semiconductor devices and (c) passive components.

self thermal impedance of semiconductor devices and passive components are shown in Fig. 11(b) and (c).

There are 19 main heat sources in the given MI. To speed up the subsequent calculation for the long-term junction temperature, the adjacent devices with the same part number and the same power loss are combined into one heat source. Thus, S_1-S_2, S_3-S_4, S_5-S_6, S_7-S_8, D_1-D_2 and C_{r1}-C_{r2} are simplified into S_{12}, S_{34}, S_{56}, S_{78}, D_{12} and C_{r12}, respectively. With the system-level FEM simulations, the junction-enclosure thermal resistance (i.e., steady-state thermal impedance) matrix also can be obtained:

$$\mathbf{R}_{je} = \begin{bmatrix}
8.5 & 0.95 & 0.3 & 0 & 0 & 0 & 0.73 & 0 & 0 & 0 & 1.1 & 0 & 0 \\
0.96 & 5 & 0.5 & 0 & 0 & 0 & 1 & 0 & 0 & 0 & 1 & 0.35 & 0 \\
0.29 & 0.5 & 4.9 & 0 & 0 & 0 & 0.34 & 0.54 & 0 & 0 & 0.31 & 1 & 0 \\
0 & 0 & 0 & 3.4 & 1.1 & 0.25 & 0 & 0 & 0.8 & 0.85 & 0 & 0 & 0.36 \\
0 & 0 & 0 & 1.1 & 3.4 & 0.16 & 0 & 0 & 0.58 & 0.7 & 0 & 0 & 0.22 \\
0 & 0 & 0 & 0.23 & 0.16 & 5.2 & 0 & 0.34 & 0.33 & 0 & 0 & 0.2 & 0.3 \\
0.72 & 1 & 0.36 & 0 & 0 & 0 & 15.5 & 0 & 0 & 0 & 0.76 & 0.3 & 0 \\
0 & 0 & 0.51 & 0 & 0 & 0.32 & 0 & 20.4 & 0 & 0 & 0 & 0.7 & 0 \\
0 & 0 & 0 & 0.8 & 0.56 & 0.32 & 0 & 0 & 5.8 & 0.73 & 0 & 0 & 0.4 \\
0 & 0 & 0 & 0.84 & 0.7 & 0 & 0 & 0 & 0.74 & 20.6 & 0 & 0 & 0.42 \\
1.1 & 1 & 0.33 & 0 & 0 & 0 & 0.74 & 0 & 0 & 0 & 2 & 0.29 & 0 \\
0 & 0.3 & 1 & 0 & 0 & 0.16 & 0.23 & 0.7 & 0 & 0 & 0.27 & 1.95 & 0 \\
0 & 0 & 0 & 0.35 & 0.21 & 0.34 & 0 & 0 & 0.4 & 0.42 & 0 & 0 & 2
\end{bmatrix} \quad (7)$$

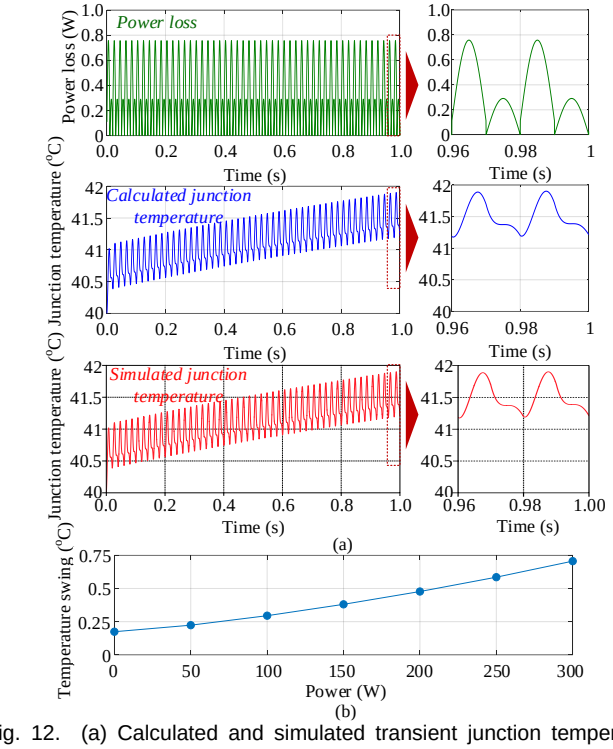

Fig. 12. (a) Calculated and simulated transient junction temperature profile for MOSFETs S_5-S_8 when the MI is modulated with unipolar PWM and injecting active power to the grid. (b) Junction temperature swing of S_5-S_8 with respect to the MI power level.

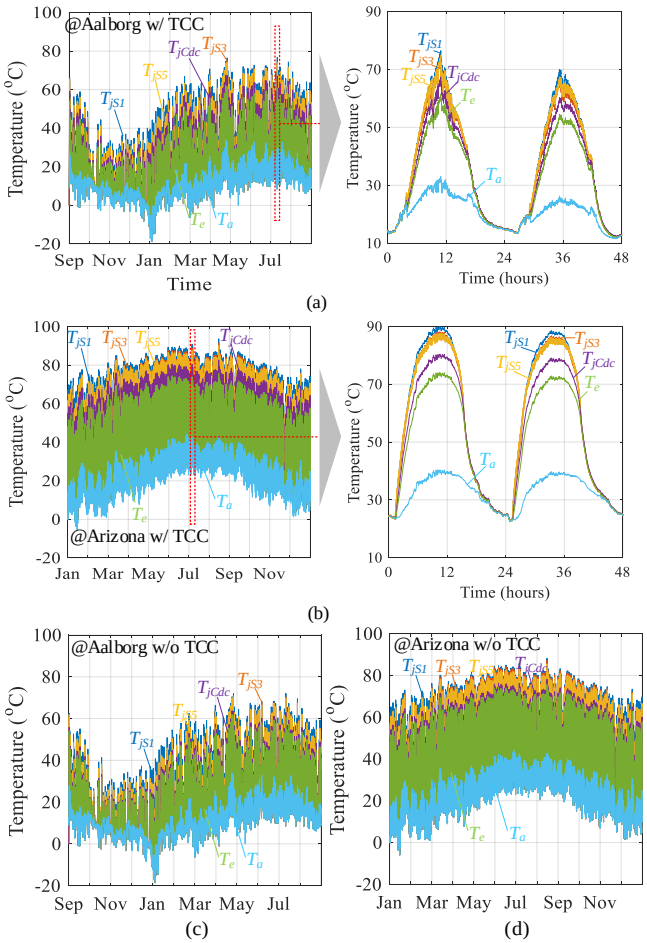

Fig. 13. Temperature profiles for critical components (S_1, S_3, S_5, C_{dc}) and the enclosure. (a) Aalborg, Denmark, considering the thermal cross-coupling (TCC); (b) Arizona, USA, considering TCC; (c) Aalborg, Denmark, not considering TCC; (d) Arizona, USA, not considering TCC.

where the diagonal elements are the self thermal resistances and the non-diagonal elements represent the mutual thermal resistances. Analyzing the degree of symmetry of (7) yields

$$S_m = \frac{|| (\mathbf{R_{je}} - \mathbf{R'_{je}}) / 2 ||}{|| (\mathbf{R_{je}} + \mathbf{R'_{je}}) / 2 ||} = 0.39\% . \quad (8)$$

This implies that the thermal resistance matrix has a fairly high degree of symmetry due to the reciprocity of heat conduction [50]-[51]. The thermal impedance Z_{jemn} can be fitted as a *Kth*-order Foster model:

$$Z_{jemn} = \sum_{k=1}^{K} R_{jemn,k}(1 - e^{-t/\tau_{jemn,k}}) \quad (9)$$

where R_{jemn} and τ_{jemn} are junction-enclosure thermal resistance and time constant between components *m* and *n*. The ambient-enclosure temperature difference and the junction temperature of component *m* can be calculated from the discrete equations:

$$\begin{cases} \Delta T_{jem}(x+1) = \sum_{n=1}^{N}\sum_{k=1}^{K}\left[\begin{array}{l}\Delta T_{jemn,k}(x)e^{-t/\tau_{mn,k}} \\ \quad + P_{l,n}(x)R_{mn,k}(1 - e^{-t/\tau_{mn,k}})\end{array}\right] \\ \Delta T_{ea}(x+1) = \Delta T_{ea}(x)e^{-t/\tau_{ea}} + P_{l,tot}(x)R_{ea}(1 - e^{-t/\tau_{ea}}) \\ T_{jm}(x+1) = \Delta T_{jem}(x+1) + \Delta T_{ea}(x+1) + T_a \end{cases} \quad (10)$$

The unipolar pulse width modulation (PWM) [52] is applied to the inverter stage, and it is assumed that only active power is injected to the grid. During the positive half cycle of the grid voltage, S_5 and the body diode of S_6 turn on alternately, and S_8 and the body diode of S_7 conduct alternately. During the negative half cycle, S_6 and the body diode of S_5 turn on alternately, and S_7 and the body diode of S_8 conduct alternately. The channel of each MOSFET conducts during a half cycle, whereas the body diode conducts during the other half cycle. The (conduction and switching) power losses of the MOSFET channel and its body diode are different, leading to an asymmetrical power loss profile for the MOSFETs in the inverter stages, as shown in Fig. 12(a). Fig. 12 also presents the calculated and simulated junction temperature profiles of S_5-S_8 for 300-W active power injected to the grid. Evidently, their junction temperature profile has 50-Hz fluctuations, which are caused by the periodical power losses at 50 Hz. The calculations agree well with simulations. The amplitude of the 50-Hz temperature swing rises with respect to the MI power increase, as indicated in Fig. 12(b).

C. Lifetime and Damage Accumulation Modeling

According to the FMEA results in [12] and [18], the progressive increase of the on-state resistance (wear-out) of MOSFETs is mainly caused by the growth of fatigue cracks and voids into the source metal layer. A 20% rise of the on-state resistance is chosen as the criteria of wear-out failure and a Coffin-Manson law based reliability model is built in [12]

$$N_f = \alpha \cdot (\Delta T_j)^{-m} \quad (11)$$

where N_f is the number of cycles to failure, ΔT_j is the junction temperature swing, and α and *m* are fitting parameters.

A widely-used capacitor lifetime model is employed for the lifespan projection of capacitors [15], [19]

$$L_{cn} = L_{c0} \cdot 2^{\frac{T_0 - T_h}{n_1}} (V / V_0)^{-n_2} \quad (12)$$

in which L_{cn} is the lifetime under the thermal and electrical stress T_h and V, L_{c0} is the lifetime under the reference temperature T_0 and the nominal voltage V_0. The coefficient n_1 is a temperature dependent constant, and n_2 is the voltage stress exponent.

For snap-in aluminum electrolytic capacitors, the temperature-dependent parameter n_1 is 10 and the voltage stress exponent n_2 is 5 when the applied voltage is 80 %-100 % of the rated voltage [53]-[54]. The temperature-dependent parameter n_1 = 10 also holds for film capacitors [15], [36], [57]. However, the voltage stress exponent n_2 for film capacitors is reported from around 7 to 9.4 in [9], [15], [36], from 5 to 10 in [55], from 7 to 12 in [56], and 7 in [57]. The discrepancy between the values may be attributed to the different technologies adopted by the different manufacturers [55]. To have an unbiased lifetime estimation of film capacitors, the median value 8.2 is adopted. For the ceramic capacitor used, the manufacturer provides the coefficients n_1 = 8, and n_2 = 3 [58].

According to the commonly used Miner's rule [59]-[60], the damage accumulates linearly:

$$D_{mg} = \sum_k (n_k / N_{fk}) \quad (13)$$

where n_k is the number of cycles with a specific thermal loading stress, and N_{fk} is the number of cycles till failure for the same stress. The device fails when the accumulated D_{mg} reaches 1.

IV. Wear-Out Failure Analysis of the Microinverter

A. Static Annual Damage of Components

The mission profiles from Aalborg, Denmark, and Arizona, USA, are applied to the electro-thermal model. Then, the junction/hotspot temperature profiles for each component and the enclosure temperature can be derived (cf. Fig. 13). The resolution is 100 points/s to accommodate 50-Hz junction temperature fluctuations of the inverter MOSFETs. If the thermal cross-coupling (TCC) effect is not considered, the junction/hotspot temperatures of components will be underestimated, as shown in Fig. 13(c) and (d). It should be noted that a MI is typically installed on the mounting rack of PV panels, and thus the real ambient temperature of the MI may be higher than the applied one which represents the open-field temperature. The PV module degradation is ignored to offset this methodology flaw.

With and without considering the TCC effect, the annual damage of each critical component at the two locations is shown in Fig. 14(a). It can be observed that the dc-link capacitor C_{dc} has the highest annual damage at both locations, i.e., 0.01 and 0.057 for Aalborg and Arizona, respectively. Assuming there are no other kinds of failures, the corresponding wear-out lifetimes of the dc-link capacitor are 100 yrs and 17.54 yrs for the two operating locations. However, if the thermal cross-coupling effect is not considered, then the annual damages of C_{dc} at the two locations are 0.007 and 0.031, which results in an underestimation rate of about 30 %. The mean ambient temperature of Arizona over a year, T_{am}, is 22.34 °C. If the solar irradiance of Arizona remains the same, but the mean ambient temperature T_a varies, then the annual damage of each component will change as well, as shown in Fig. 14(b). It can be seen that the annual damages of capacitors rise significantly with respect to the increase of T_{am}, while the damages of semiconductors increase slightly. This results from (11) where the number of cycles to failure is mainly dependent on the junction temperature swing instead of its mean value.

This article has been accepted for publication in a future issue of this journal, but has not been fully edited. Content may change prior to final publication. Citation information: DOI 10.1109/TIE.2018.2831643, IEEE Transactions on Industrial Electronics

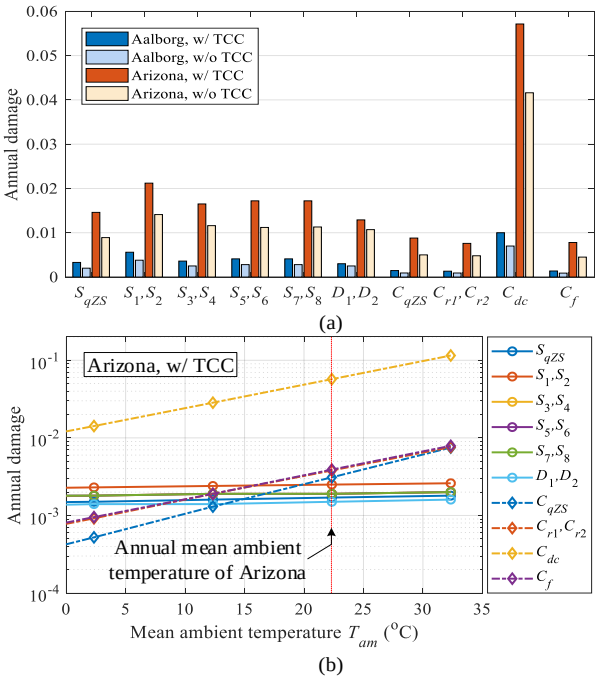

Fig. 14. Annual damage to each critical component. (a) Annual damage when the MI operates at different locations with and without considering the thermal cross-coupling (TCC). (b) Annual damage of each component versus the mean ambient temperature in Arizona.

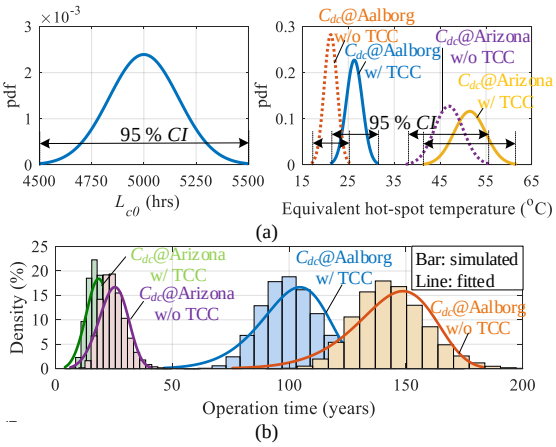

Fig. 15. (a) Probability density functions of the parameters for the dc-link capacitor C_{dc}; (b) Histograms of years to wear-out failure for a population of 1×10^5 capacitor samples operating at two locations, with and without considering the TCC effect.

B. Monte Carlo Simulation and System Failure Probability Due to Wear-out

There are some uncertainties which may affect the MI lifetime in the real-world operation. First, the parameters in the lifetime model could vary. For instance, the applied lifetime model for MOSFETs is derived from the testing data in [12], and the parameters α and m have boundaries. Second, the parameters of the employed devices vary, which is caused by the manufacturing process variations among the devices with the same part number. According the datasheet, the on-state resistances of the MOSFETs employed in the two stages vary within ±20% and ±10%, respectively. Third, the mission profile could also vary due to the climate change.

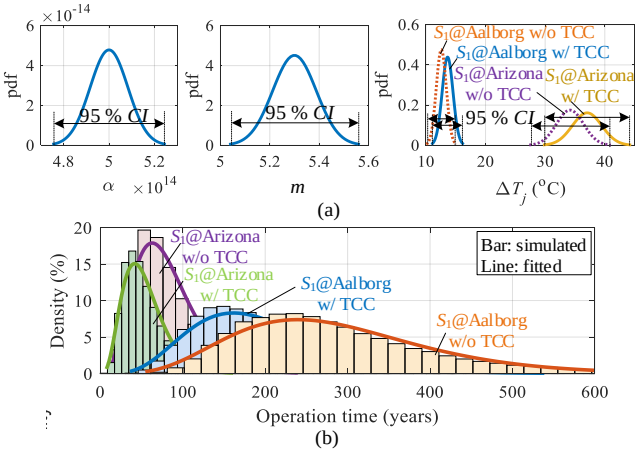

Fig. 16. (a) Probability density functions of the parameters for S_1; (b) Histograms of years to wear-out failure for a population of 1×10^5 samples operating at two locations, with and without considering the TCC effect.

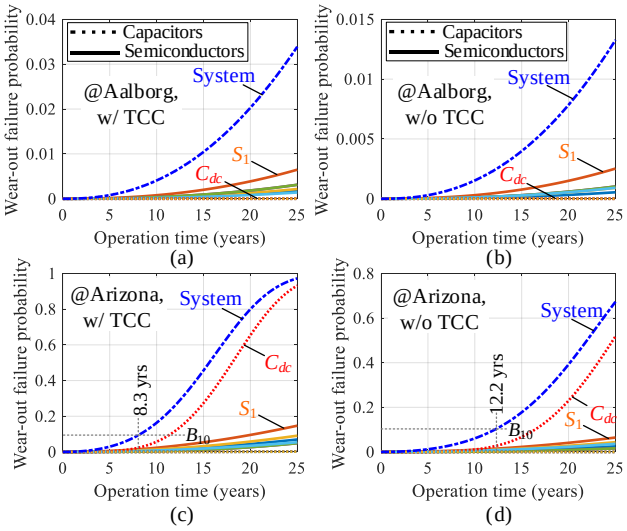

Fig. 17. Probability curves of wear-out failure for each component and the system when operating at (a) Aalborg, Denmark, with considering the thermal cross-coupling (TCC) effect; (b) Aalborg, Denmark, without considering the TCC effect o; (c) Arizona, US, with considering the TCC effect; (d) Arizona, US, without considering the TCC effect.

It is assumed that all the variations mentioned above obey the normal distribution. The second and third types of uncertainties (e.g., $R_{ds,on}$ of MOSFET, ESR of capacitor, ambient temperature, and solar irradiance) directly affect the junction/hotspot temperature. Hence, the junction/hotspot temperature swing will vary within a certain range. The probability density functions (pdfs) of the parameters of C_{dc} and S_1 are shown in Figs. 15(a) and 16(a), considering a 95% confidence interval (CI). For other devices, their parameters variations are also considered.

To analyze the impact of all the uncertainties on the system wear-out failure, the continuous mission profile should be converted into an equivalent static one, which produces the same degradation [61]. Then a sensitivity analysis—Monte Carlo simulation can be carried out by simultaneously taking into account all parameter variations. The population number for each sample is 1×10^5 in the Monte Carlo simulation. The histograms of years to wear-out failure for the selected

This article has been accepted for publication in a future issue of this journal, but has not been fully edited. Content may change prior to final publication. Citation information: DOI 10.1109/TIE.2018.2831643, IEEE Transactions on Industrial Electronics

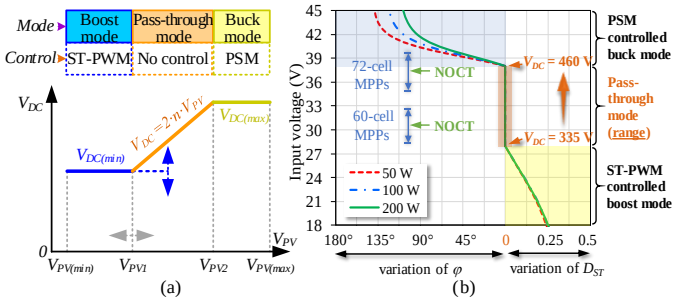

Fig. 18. Advanced multi-mode control of the qZSSRC with a variable dc-link voltage: (a) sketch of dc-link voltage variations; (b) regulation characteristics.

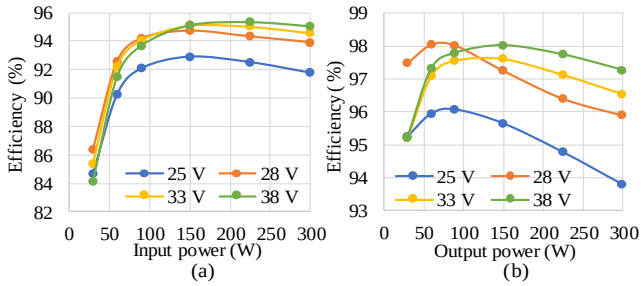

Fig. 19. Measured efficiency with the new control strategy: (a) the whole PV MI incl. the auxiliary power, (b) the dc-dc power stage.

components, C_{dc} and S_5, are shown in Figs. 15(b) and 16(b), respectively, which are fitted with the Weibull distribution [61]:

$$f(t)=\frac{\beta}{\eta}\left(\frac{t}{\eta}\right)^{\beta-1}e^{-\left(\frac{t}{\eta}\right)^{\beta}},\ F(t)=1-e^{-\left(\frac{t}{\eta}\right)^{\beta}} \tag{14}$$

where β is the shape parameters and η is the scale parameter.

Assume all the considered devices are connected in series in the reliability model, i.e., any component failure will lead to system failure. Then the system wear-out failure $F_{sys}(t)$ equals:

$$F_{sys}(t)=1-\prod(1-F_i(t)) \tag{15}$$

where $F_i(t)$ represents the cumulative distribution function (cdf) of the component wear-out failure.

Fig. 17 shows the probability curves of wear-out failures for components and the system when operating at Aalborg, Denmark, and Arizona, US, with and without considering the thermal cross-coupling effect. First, it can be seen that the mission profile has a strong impact on the wear-out failure: when operating in a harsher environment, i.e., Arizona, the wear-out failure probabilities before 25-year operation are significantly higher. Second, neglecting the thermal cross-coupling effect will lead to an obvious underestimation of the wear-out failure probability; when operating at Aalborg, the predicted system wear-out failure probability before 25 years is 3.34 % (cf. Fig. 17(a)), whereas the corresponding value is only 1.3 % (cf. Fig. 17(b)) if neglecting the thermal cross-coupling effect. When operating at Arizona, the B_{10} lifetimes with and without considering the thermal cross-coupling effect are 8.3 yrs and 12.2 yrs (cf. Fig. 17(c) and (d)), respectively, which implies that about 45 % lifetime overestimation can be made if neglecting the thermal cross-coupling effect. In addition, it can be seen that the dc-link electrolytic capacitor C_{dc} has the highest wear-out failure probability when the operating environment is harsh, and thus dominates the system wear-out failure. Hence, it can be concluded that the dc-link electrolytic capacitor C_{dc} is the bottleneck of 25-year reliable operation for the studied PV MI.

V. Reliability Improvement of the Microinverter

It can be concluded from the reliability evaluation results (cf. Fig. 17) that the 25-year wear-out failure probability of the studied PV microinverter is high when operating in a harsh environment—Arizona, US. Therefore, measures will be taken to improve its reliability.

A. Advanced Multi-Mode Control of the qZSSRC

The multi-mode control of the qZSSRC [26] results in the operation in the pass through mode (PTM) only at the particular voltage where (1) holds true for the fixed dc-link voltage. The PTM corresponds to the peak efficiency. However, it is not necessary for the grid-tied microinverter to have a stable dc-link voltage. Hence, an advanced multi-mode control with a variable dc-link voltage (cf. Fig. 18(a)) could be implemented on the qZSSRC to cover the voltage ranges of the most probable maximum power points (MPPs) of the 60- and 72-cell Silicone (Si) PV modules in PTM, as shown in Fig. 18(b). The lower bound of the PTM range is defined by the peak grid voltage $V_{g(pk)}$ with an assumption that the dc-link voltage is 10 V above that:

$$V_{PV1}=\frac{V_{g(pk)}+10}{2n} \tag{16}$$

The grid RMS voltage is usually within the range of 207 V to 253 V, which results in possible variations of the minimum dc-link voltage $V_{DC(min)}$ from 305 V to 370 V. For the rated grid voltage of 230 V, this voltage equals $V_{DC(min)}$ = 335 V. The upper bound of the PTM is limited by the voltage rating of the dc-link capacitor. Considering the existing technology, the electrolytic capacitor rated voltage of 500 V could be recommended. Assuming $V_{DC(max)}$ = 460 V, then a safety margin of 40 V is achieved:

$$V_{PV2}=\frac{V_{DC(\max)}}{2n} \tag{17}$$

The PTM is active between V_{PV1} = 28 V and V_{PV2} = 38 V for the nominal grid RMS voltage of 230 V. The control characteristic of the qZSSRC shown in Fig. 18(b) at the nominal grid voltage features a considerable PTM range owing to the proposed advanced multi-mode control. Remarkably, the PTM overlaps with the ranges of the most probable MPPs of the 60- and 72-cell Si PV modules over the temperature variations between 30 °C and 60 °C. This also includes the standard nominal operating cell temperature (NOCT) of 45 °C. The MPPs outside the PTM correspond to the temperatures that are rarely observed in practice.

The advanced multi-mode control with a variable DC-link voltage results in an efficiency improvement by over 2% for the PV microinverter, as shown in Fig. 3 and Fig. 19. This means that the power losses and the junction/hotspot temperatures of components will be reduced, which is beneficial for reliability improvement.

B. Long-Lifetime DC-Link Electrolytic Capacitor

From Fig. 17(c), it is seen that the long-term (e.g., 25 years) reliability bottleneck of the PV microinverter operating in a harsh environment is the dc-link electrolytic capacitor C_{dc}. Therefore, C_{dc} should be selected carefully. In the baseline

This article has been accepted for publication in a future issue of this journal, but has not been fully edited. Content may change prior to final publication. Citation information: DOI 10.1109/TIE.2018.2831643, IEEE Transactions on Industrial Electronics

design, the dc-link employs a cost-optimized 150-μF electrolytic capacitor, whose nominal lifetime is 5000 hours at 85 °C. To decrease the wear-out failure probability, an emerging high-reliability electrolytic capacitor (ESR at 100 Hz at 25°C: 0.54 Ω, nominal lifetime: 5000 hours @105°C), will be used in the new design along with the variable DC-link voltage control.

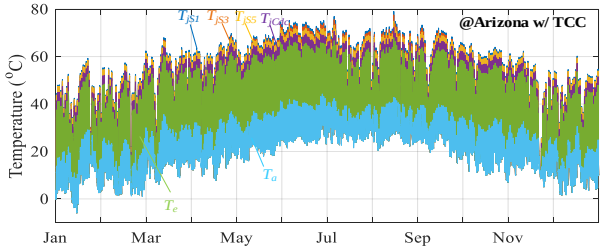

Fig. 20. Calculated temperature profiles of critical components (S_1, S_3, S_5, C_{dc}) and the enclosure of the PV microinverter with the variable dc-link voltage control when operating in Arizona, US.

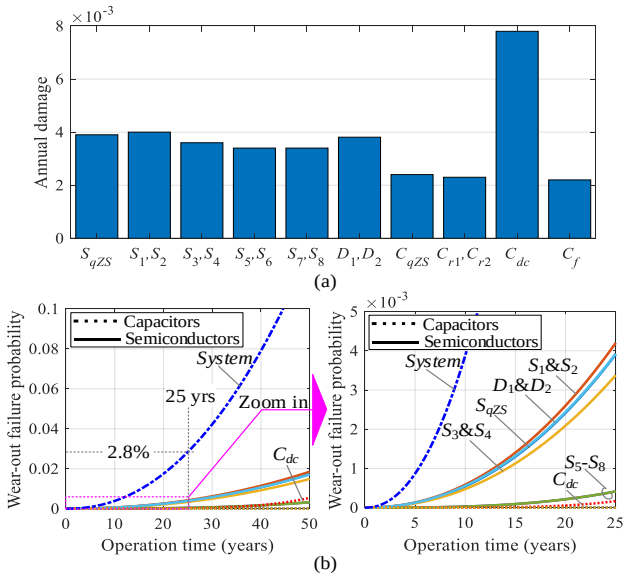

Fig. 21. Reliability evaluation results of the PV microinverter with the variable dc-link voltage control and the new electrolytic capacitor; the mission profile of Arizona is applied: (a) annual damage and (b) wear-out failure probabilities of each component and the system.

C. Wear-Out Failure Probability Estimation

With the advanced multi-mode control and the new DC-link capacitor, the temperatures of the selected critical components (S_1, S_3, S_5, C_{dc}) and the enclosure can be obtained, as shown in Fig. 20. Compared with the baseline solution, the new design enables the microinverter to operate at lower temperatures (cf. Fig. 13 and Fig. 20); the maximum temperature reduction is about 14 °C. The reliability evaluation procedure is repeated for the new design, and the results are shown in Fig. 21. It is seen from Figs. 14(a) and 21(a) that the annual damage to each component is decreased due to the lower junction/hotspot temperature. Particularly, the annual damage to the dc-link capacitor C_{dc} is significantly reduced from 0.057 to 0.0078 because of the lower hotspot temperature and longer nominal capacitor lifetime. Fig. 21(b) shows the probability curves of wear-out failure for the components and the system. As can be observed, the 25-year wear-out failure probability of each component is kept at a low level. The wear-out failure probabilities over time obey the Weibull distribution, but the shape parameters of the capacitors are larger than those of the semiconductors, as illustrated in Fig. 21(b). Therefore, at the early stage of life cycle, the system wear-out failure is dominated by semiconductors. Nevertheless, the system wear-out failure probability over 25-year operation is about 2.8 %, which is a dramatic improvement compared to the baseline solution (cf. Fig. 17(c)).

VI. Conclusions

The wear-out performance of a 300-W PV microinverter is evaluated by applying different mission profiles, experimental measurements, system-level FEM simulations, Monte Carlo simulation, and Weibull analysis. Harsh operating conditions of microinverters compel the enclosure to be filled up with thermally conducting casting compound, causing a strong thermal cross-coupling effect between components. The performed analysis reveals that: 1) the mission profile has a significant impact on the system wear-out failure; 2) neglecting the thermal cross-coupling effect will lead to a remarkable underestimation of the system wear-out failure probability; 3) the DC-link electrolytic capacitor is the bottleneck for the long-term (e.g., 25-year) reliable operation of the studied PV microinverter. In order to reduce the system wear-out failure probability, the variable DC-link voltage control is applied and the original cost-optimized DC-link capacitor is replaced with a more reliable aluminum electrolytic capacitor. It is shown that the probability of system failure due to wear-out over 25 years can be significantly reduced with the new design.

Nevertheless, the reliability evaluation results need to be treated cautiously. The aim of the wear-out failure probability prediction is to identify the weakest link in the PV micro-inverter, and to benchmark different modulation/control/design techniques for reliability improvement. The wear-out failure probability in real operation may differ from the estimation in this paper due to several limitations: 1) the applied empirical device lifetime models are derived by accelerated testing at a specific condition and may lead to errors due to different operating conditions; 2) depending on the installation position of the microinverter, its real ambient temperature may be much higher than the open-field ambient temperature; 3) the degradation of PV modules will slow down the wear-out of microinverters; 4) in addition to wear-out, there are also other failure modes (cf. Fig. 4) which may affect the hardware failure, but are not taken into account in this paper.

Acknowledgment

The authors would like to thank Ubik Solutions LLC for the support of this research.

References

[1] L. Tinker and R. Jones-Albertus, “Emerging PV technologies: The path to market competitiveness,” *2016 IEEE 43rd Photovoltaic Specialists Conference (PVSC)*, Portland, OR, 2016, pp. 3471-3474.

[2] R. M. Burkart and J. W. Kolar, “Comparative Life Cycle Cost Analysis of Si and SiC PV Converter Systems Based on Advanced η-ρ-σ Multiobjective Optimization Techniques,” *IEEE Trans. on Power Electron.*, vol. 32, no. 6, pp. 4344-4358, June 2017.

[3] H. Oldenkamp, I. de Jong, “The return of the ac-module inverter,” *in Proc. 24th Eur. Conf. Photovolt. Solar Energy*, Hamburg, 2009, pp. 3101–3104.

[4] S. B. Kjaer, J. K. Pedersen, and F. Blaabjerg, “A review of single phase grid-connected inverters for photovoltaic modules,” *IEEE Trans. Ind. Appl.*, vol. 41, no. 5, pp. 1292–1306, Oct. 2005.

[5] D. Leuenberger and J. Biela, "PV-Module Integrated AC Inverters (AC Modules) with Subpanel MPP-Tracking," *IEEE Trans. Power Electron*., vol. 32, no. 8, pp. 6105–6118, 2017.

[6] J. Flicker, G. Tamizhmani, M. K. Moorthy, R. Thiagarajan, and R. Ayyanar, "Accelerated testing of module-level power electronics for long-term reliability," *IEEE J. Photovolt.*, vol. 7, no. 1, pp. 259–267, Jan. 2017.

[7] B. Gu, "Power converter and control design for high-efficiency electrolyte-free microinverters," Ph.D. dissertation, Blacksburg, VA, Nov. 2013.

[8] M. A. Maehlum,"*The Real Lifespan of Solar Panels*," available online [2017], http://energyinformative.org/lifespan-solar-panels/.

[9] P. Hacke, et al., "A status review of photovoltaic power conversion equipment reliability, safety, and quality assurance protocols," *Renewable and Sustainable Energy Reviews*, pp. 1097-1112, Feb. 2018.

[10] H. Wang, et al., "Transitioning to physics-of-failure as a reliability driver in power electronics," *IEEE J. Emerg. Sel. Topics Power Electron.*, vol. 2, no. 1, pp. 97–114, Mar. 2014.

[11] R. Bayerer, T. Herrmann, T. Licht, J. Lutz, and M. Feller, "Model for power cycling lifetime of IGBT modules - various factors influencing lifetime," *in Proc. of Integrated PowerSystems (CIPS) 2008*, pp.1-6, 2008.

[12] A. Testa, S. De Caro, and S. Russo, "A reliability model for power MOSFETs working in avalanche mode based on an experimental temperature distribution analysis," *IEEE Trans. Power Electron.*, vol. 27, no. 6, pp. 3093-3100, Jun. 2012.

[13] Y. Song and B. Wang, "Survey on reliability of power electronic systems," *IEEE Trans. Power Electron*., vol. 28, no. 1, pp. 591–604, Jan. 2013.

[14] H. Wang, M. Liserre, and F. Blaabjerg, "Toward reliable power electronics: Challenges, design tools, and opportunities," *IEEE Ind. Electron. Mag*., vol. 7, no. 2, pp. 17–26, Jun. 2013.

[15] H. Wang, and F. Blaabjerg, "Reliability of capacitors for DC link applications in power electronic converters—an overview," *IEEE Trans. Ind. Appl.*, vol. 50, no. 5, pp. 3569-3578, Sep. 2014.

[16] M. Musallam, C. Yin, C. Bailey, and M. Johnson, "Mission profile-based reliability design and real-time life consumption estimation in power electronics," *IEEE Trans. Power Electron*., vol. 30, no. 5, pp. 2601–2613.

[17] P. D. Reigosa, H. Wang, Y. Yang, and F. Blaabjerg, "Prediction of bond wire fatigue of IGBTs in a PV inverter under a long-term operation," *IEEE Trans. Power Electron*., vol. 31, no. 10, pp. 7171–7182, Oct. 2016.

[18] S. Russo, et al. "Reliability assessment of power MOSFETs working in avalanche mode based on a thermal strain direct measurement approach," *IEEE Trans. Ind. Appl.*, vol. 52, no. 2, pp. 1688-1697, Mar./Apr. 2016.

[19] D. Zhou, H. Wang, and F. Blaabjerg, "Mission profile based system-level reliability analysis of DC/DC converters for a backup power application," *IEEE Trans. Power Electron*., vol. PP, no. 99, pp. 1-1., 2017.

[20] S. Harb and R. S. Balog, "Reliability of candidate photovoltaic module integrated-inverter (PV-MII) topologies: A usage model approach," *IEEE Trans. Power Electron.*, vol. 28, no. 6, pp. 3019–3027, Jun. 2013.

[21] G. TamizhMani, "Standardization and Reliability Testing of Module-Level Power Electronics (MLPE)," NREL, 2015.

[22] *Military Handbook: Reliability Prediction of Electronic Equipment*, MIL-HDBK-217F, 1991.

[23] S. Kouro, J. Leon, D.Vinnikov, L.Franquelo, "Grid-connected photovoltaic systems: an overview of recent research and emerging PV converter technology," *IEEE Ind. Electron. Mag*., vol.9, no.1, pp.47-61, Mar. 2015.

[24] Y. Shi, Y. Li, T. Kayiranga and H. Li, "Exploring the LCL characteristics in GaN Based Single-L Quasi-Z-Source Grid-tied Inverters," *IEEE Trans. Ind. Electron*., vol. 64, no. 10, pp. 7758-7768, Oct. 2017.

[25] D. Sun, B. Ge, W. Liang, H. Abu-Rub, F. Z. Peng, "An energy stored quasi-Z-source cascade multilevel inverter-based photovoltaic power generation system," *IEEE Trans. Ind. Electron*., vol. 62, no. 9, pp. 5458–5467, 2015.

[26] D. Vinnikov, A. Chub, L. Liivik, and I. Roasto, "High-performance quasi-Z-source series resonant DC-DC converter for photovoltaic module level power electronics applications," *IEEE Trans. Power Electron*., vol. 32, no. 5, pp. 3634-3650, May 2017.

[27] D. Vinnikov, R. Kosenko, A. Chub and E. Liivik, "Shade-tolerant photovoltaic microinverter with time adaptive seamless P-V curve sweep MPPT," *19th European Conference on Power Electronics and Applications (EPE'17 ECCE Europe)*, Warsaw, Poland, 2017, pp. 1-8.

[28] A. Chub, L. Liivik, D. Vinnikov and J. Zakis, "Asymmetrical PWM control of galvanically isolated impedance-source series resonant DC-DC converters," *10th Int. Conf. Compt., Power Electron. Power Eng. (CPE-POWERENG)*, Bydgoszcz, 2016, pp. 341-346.

[29] H. Cha, F. Z. Peng and D. Yoo, "Z-source resonant DC-DC converter for wide input voltage and load variation," *The 2010 International Power Electronics Conference - ECCE Asia -*, Sapporo, 2010, pp. 995-1000.

[30] A. Chub, D. Vinnikov, R. Kosenko, E. Liivik, "Wide input voltage range Photovoltaic microconverter with reconfigurable buck-boost switching stage*," IEEE Trans. Ind. Electron.*, vol. 64, no. 7, pp. 5974-5983, 2017.

[31] K. M. Matsuishi and T. Endo, "Fatigue of metals subjected to varying stress," *Jap Soc. Mech. Eng*., pp. 37-40, Mar. 1968.

[32] W. Konrad, G. Deboy, and A. Muetze, "A power supply achieving titanium level efficiency for a wide range of input voltages," *IEEE Trans. Power Electron*., vol. 32, no. 1, pp. 117–127, Jan. 2017.

[33] Datasheet: C4D02120E SiC Schottky Diode, available online [2017]: http://www.wolfspeed.com/media/downloads/128/C4D02120E.pdf

[34] H. Wang, Y. Yang, and F. Blaabjerg, "Reliability-oriented design and analysis of input capacitors in single-phase transformer-less photovoltaic inverters," *in Proc. of APEC'13*, pp. 2929-2933, Mar. 2013.

[35] Y. Shen, H. Wang, and F. Blaabjerg, "Reliability Oriented Design of a Grid-Connected Photovoltaic Microinverter," *in Proc. IFEEC-ECCE Asia 2017*, pp. 1-6, Jun. 2017.

[36] Emerson Network Power, Capacitors age and capacitors have an end of life, White Paper.

[37] "General description of aluminum electrolytic capacitors", available online [2017]: http://www.nichicon.co.jp/english/products/pdf/aluminum.pdf.

[38] TDK, "Aluminum Electrolytic Capacitors General technical information," Available online [2017]: https://de.tdk.eu/download/185386/5f33d2619fa73419e2a4af562122e90c/pdf-generaltechnicalinformation.pdf

[39] Vishay, "Characteristics and Definitions used for Film Capacitors," Available online [2017]: https://www.vishay.com/docs/28147/intro.pdf.

[40] TDK, "Film Capacitors General technical information," Available online [2017]: https://en.tdk.eu/download/530754/bb7f3c742f09af6f8ef473fd34f6000e/pdf-generaltechnicalinformation.pdf

[41] CDE Cornell Dubilier, "Multilayer Ceramic Capacitors - Performance Characteristics," Available online [2017]: http://www.cde.com/resources/catalogs/ceramperf.pdf

[42] K. Venkatachalam, C. R. Sullivan, T. Abdallah, H. Tacca, "Accurate prediction of ferrite cores loss with nonsinusoidal waveforms using only Steinmetz parameters," in *Proc. IEEE Workshop Comput. Power Electron.*, 2002, pp. 36–41.

[43] P. L. Dowell, "Effects of eddy currents in transformer windings," in *Proc. Inst. Elect. Eng.*, Aug. 1966, vol. 113, no. 8, pp. 1387–1394.

[44] J. Ferreira, "Improved analytical modeling of conductive losses in magnetic components," *IEEE Trans. Power Electron.*, vol. 9, no. 1, pp. 127–131, Jan. 1994.

[45] Ferroxcube, "3C95 Material specification," available online [2017]: https://www.ferroxcube.com/upload/media/product/file/MDS/3c95.pdf.

[46] Stobicast® L 781.36, available online [2017], http://www.chemsol.co.il/files/TDS/Stobicast/TDS_L781.36.pdf

[47] K.Azar, "Thermal measurements in electronics cooling", CRC Press. 1997.

[48] Y. A. Cengel, R H. Turner, J. M. Cimbala, and M. Kanoglu. Fundamentals of thermal-fluid sciences. New York, NY: McGraw-Hill, 2008.

[49] X. Hu, S. Lin, S. Stanton, and W. Lian, "A Foster Network Thermal Model for HEV/EV Battery Modeling," *IEEE Trans. Industry Appl*., vol. 47, no. 4, p. 1692-1699, Jul./Aug. 2011.

[50] D. Billings, and R. Stout, "Using linear superposition to solve multiple heat source transient thermal problems", *ASME. Int. Electronic Packaging Technical Conf. and Exhibition*, vol. 2, pp. 791-799, 2007.

[51] K. Olesen, "Transient thermal analysis of complex systems by linear superposition," *ECPE Workshop Thermal and Reliability Modelling and Simulation of Power Electronics Components and Systems*, Fuerth/Nuremberg, Germany, Nov. 2016.

[52] R.-S. Lai and K. D. T. Ngo, "A PWM method for reduction of switching loss in a full-bridge inverter," *IEEE Trans. Power Electron*., vol. 10, no. 3, pp. 326–332, May 1995.

[53] S. G. Parler, "Deriving life multipliers for electrolytic capacitors," *IEEE Power Electron. Soc. Newsl.*, vol. 16, no. 1, pp. 11–12, Feb. 2004.

[54] A. Albertsen, "*Electrolytic capacitor lifetime estimation*," [Online 2017]. Available: www.jianghai-america.com.

[55] R. Gallay. "Metallized Film Capacitor Lifetime Evaluation and Failure Mode Analysis," in *Proc. CAS-CERN Accelerator School: Power Converters*, Baden, Switzerland, 7–14 May 2014, pp. 1-12.

[56] Z. Li, H. Li, F. Lin, Y. Chen, D. Liu, B. Wang, H. Li, and Q. Zhang, "Lifetime investigation and prediction of metallized polypropylene film capacitors," *Microelectron. Rel*., vol. 53, no. 12, pp. 1962–1967, Jun. 2013.

[57] Illinois Capacitor, Inc. Capacitor lifetime calculator, [online]. Available: http://www.illinoiscapacitor.com/tech-center/life-calculators.aspx

[58] muRata, "Ceramic Capacitors FAQ," Available online [2017] http://www.murata.com/support/faqs/products/capacitor/mlcc/qlty/0010

[59] M. Miner, "Cumulative damage in fatigue," *J. Appl. Mech.*, vol. 12, pp. 159–164, 1945.

[60] M. F. Ashby and D. R. H. Jones, Engineering Materials 1—An Introduction to Properties, Applications and Design, 3rd ed. Oxford, U.K: Butterworth–Heinemann.
[61] J. McPherson, Reliability Physics and Engineering, 2nd ed. Switzerland: Springer Int., 2013.

Yanfeng Shen (S'16) received the B.S. and M.S. degrees in electrical engineering and power electronics from Yanshan University, Qinhuangdao, China, in 2012 and 2015, respectively. He is currently working toward the Ph.D. degree in power electronics at the Center of Reliable Power Electronics (CORPE), Aalborg University, Aalborg, Denmark.

He worked as an Intern at ABB Corporate Research Center, Beijing, China, from Aug. to Oct., 2015. His research interests include the reliability of power electronics, dc-dc converters and PV inverters.

Andrii Chub (S'12–M'17) received the B.Sc. degree in Electronics and M.Sc. degree in Electronic Systems from Chernihiv State Technological University, Chernihiv, Ukraine, in 2008 and 2009 respectively. In 2016, he received the Ph.D. degree in Electrical Engineering from Tallinn University of Technology.

He is employed as a Junior Researcher at the Department of Electrical Engineering, Tallinn University of Technology, Tallinn, Estonia. He has co-authored more than 40 papers and a book chapter on power electronics and applications. In addition, he holds several patents and utility models. His research interests include dc-dc and dc-ac converters, impedance source electric energy conversion technology, implementation of the new wide bandgap semiconductors in power electronic converters, renewable energy conversion systems for energy efficient residential buildings, and converter topologies for intelligent transformers.

Huai Wang (M'12, SM'17) received the B.E. degree in electrical engineering, from Huazhong University of Science and Technology, Wuhan, China, in 2007 and the Ph.D. degree in power electronics, from the City University of Hong Kong, Hong Kong, in 2012. He is currently an Associate Professor and a Research Thrust Leader in the Center of Reliable Power Electronics (CORPE), Aalborg University, Aalborg, Denmark. He was a Visiting Scientist with the ETH Zurich, Switzerland, from Aug. to Sep. 2014, and with the Massachusetts Institute of Technology (MIT), USA, from Sep. to Nov. 2013. He was with the ABB Corporate Research Center, Switzerland, in 2009. His research addresses the fundamental challenges in modelling and validation of power electronic component failure mechanisms, and application issues in system-level predictability, condition monitoring, circuit architecture, and robustness design. He has contributed a few concept papers in the field of power electronics reliability, hold 2 patents and filed 5 patents on advanced passive component concepts, and co-edited a book.

Dr. Wang received the Richard M. Bass Outstanding Young Power Electronics Engineer Award from the IEEE Power Electronics Society in 2016, and the Green Talents Award from the German Federal Ministry of Education and Research in 2014. He is currently the Award Chair of the Technical Committee of the High Performance and Emerging Technologies, IEEE Power Electronics Society. He serves as an Associate Editor of IET POWER ELECTRONICS, IEEE JOURNAL OF EMERGING AND SELECTED TOPICS IN POWER ELECTRONICS, and IEEE TRANSACTIONS ON POWER ELECTRONICS.

Dmitri Vinnikov (M'07–SM'11) received the Dipl.Eng., M.Sc., and Dr.Sc.techn. degrees in electrical engineering from Tallinn University of Technology, Tallinn, Estonia, in 1999, 2001, and 2005, respectively.

He is currently the Head of the Power Electronics Group, Department of Electrical Power Engineering and Mechatronics, Tallinn University of Technology (Estonia) and a Guest Researcher at the Institute of Industrial Electronics and Electrical Engineering, Riga Technical University (Latvia). He is the Head of R&D and co-founder of Ubik Solutions LLC - Estonian start-up company dedicated to innovative & smart power electronics for renewable energy systems. Moreover, he is one of the founders and leading researchers of ZEBE – Estonian Centre of Excellence for zero energy and resource efficient smart buildings and districts. He has authored or coauthored two books, five monographs and one book chapter as well as more than 200 published papers on power converter design and development and is the holder of numerous patents and utility models in this field. His research interests include applied design of power electronic converters and control systems, renewable energy conversion systems (photovoltaic and wind), impedance-source power converters, and implementation of wide bandgap power semiconductors.

Elizaveta Liivik (S'12–M'16) received Dipl.-Eng, M.Sc. and Ph.D. degrees in Electrical Engineering from the Department of Electrical Drives and Power Electronics, Tallinn University of Technology, Tallinn, Estonia, in 1998, 2000, and 2015, respectively.

She is currently a Researcher at the Department of Electrical Engineering, Tallinn University of Technology. From 2002 to 2007, she was a lecturer in the Department of Electrical Drives and Power Electronics, Tallinn University of Technology. Her main research interests include impedance-source power electronic converters, renewable energy and distributed generation, as well as control and reliability issues of power electronic converters in active distribution networks. She has authored or co-authored more than 25 research papers and 1 book.

Frede Blaabjerg (S'86–M'88–SM'97–F'03) was with ABB-Scandia, Randers, Denmark, from 1987 to 1988. From 1988 to 1992, he got the PhD degree in Electrical Engineering at Aalborg University in 1995. He became an Assistant Professor in 1992, an Associate Professor in 1996, and a Full Professor of power electronics and drives in 1998. From 2017 he became a Villum Investigator.

His current research interests include power electronics and its applications such as in wind turbines, PV systems, reliability, harmonics and adjustable speed drives. He has published more than 500 journal papers in the fields of power electronics and its applications. He is the co-author of two monographs and editor of 7 books in power electronics and its applications.

He has received 24 IEEE Prize Paper Awards, the IEEE PELS Distinguished Service Award in 2009, the EPE-PEMC Council Award in 2010, the IEEE William E. Newell Power Electronics Award 2014 and the Villum Kann Rasmussen Research Award 2014. He was the Editor-in-Chief of the IEEE TRANSACTIONS ON POWER ELECTRONICS from 2006 to 2012. He has been Distinguished Lecturer for the IEEE Power Electronics Society from 2005 to 2007 and for the IEEE Industry Applications Society from 2010 to 2011 as well as 2017 to 2018. In 2018 he is President Elect of IEEE Power Electronics Society. He is nominated in 2014, 2015, 2016 and 2017 by Thomson Reuters to be between the most 250 cited researchers in Engineering in the world. In 2017 he became Honoris Causa at University Politehnica Timisoara (UPT), Romania.